Journal of Materials Chemistry A

Accepted Manuscript

ROYAL SOCIETY OF CHEMISTRY

www.rsc.org/materialsA

TOC Graphic

Title: Superhydrophobic CuO nanoneedle-covered copper surfaces for anticorrosion

Authors: Feng Xiao, Shaojun Yuan,* Bin Liang, Guanqiu Li, Simo O Pehkoen, TieJun Zhang

The anodic CuO nanoneedle array films were synthesized and modified by fluorosilanization to create superhydrophobic surfaces for effective corrosion protection.

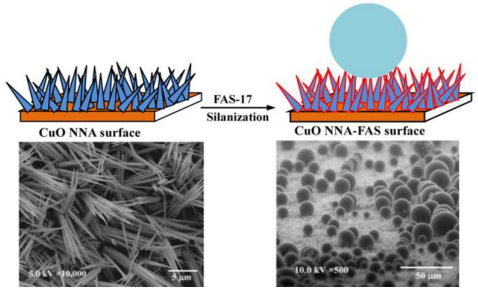

Cite this: DOI: 10.1039/c0xx00000x

www.rsc.org/xxxxxx

ARTICLE

Superhydrophobic CuO Nanoneedle-covered Copper Surfaces for Anti-corrosion

Feng Xiao,[a] Shaojun Yuan,[a,*] Bin Liang,[a] Guanqiu Li,[b] Simo Olavi Pehkonen[c] TieJun Zhang[b,*]

Received (in XXX, XXX) Xth XXXXXXXXX 2014, Accepted Xth XXXXXXXXX 20XX
DOI: 10.1039/b000000x

With the unique water-repellency and self-cleaning properties, superhydrophobic surfaces promise great potential of anticorrosion for engineered metals. The current study reported a facile and controllable anodization approach to fabricate superhydrophobic CuO nanoneedle array (NNA) films for the enhancement of corrosion resistance of copper substrates. The anodic CuO NNA films were grown on the copper foils by electrochemical anodization in an aqueous KOH solution for different anodization time. The morphological features and crystalline structures of the anodic CuO NNA were characterized by SEM-EDS and XRD. The superhydrophobicity on the hierarchical CuO NNA films was achieved by chemical modification with fluoroalkyl-silane (FAS-17). The presence of low surface energy fluorosilanized carbon (-CFx) groups on the FAS-modified surfaces was ascertained by EDS, XPS and water contact angle analyses. The wetting behaviour of the FAS-modified surfaces was investigated to elucidate the correlation between the static water contact angles, surface roughness, dynamic water contact angle hysteresis, and anodization time. The FAS-modified copper surfaces demonstrated not only the desirable superhydrophobicity with water contact angle as high as approximately 169^o and contact angle hysteresis as low as about 5^o, but also substantially improved corrosion resistance in aqueous NaCl solution (3.5%) with inhibition efficiency higher than 90%, as revealed by means of Tafel plots and EIS measurements. The stability and durability of the superhydrophobic FAS-modified surfaces was evaluated by observing the change in surface wettability and geometric microstructures as a function of exposure time in aqueous NaCl solution.

1. Introduction

Due to the superior electrical and thermal conductivity, mechanical workability, malleability and relatively noble properties, copper has been utilized in a wide range of applications, such as conductor in electrical power lines, municipal and industrial water pipelines, heat conductors and heat exchangers.[1] However, copper as an active metal is readily susceptible to corrosion, especially in an aggressive medium containing chloride (Cl^-) anions,[2] thus leading to a compromised service lifespan. This poses a serious threat to industrial economy and potential danger to human health. Hence, corrosion control of copper has become an important subject worthy of intensive investigation.

Various strategies, such as cathodic protection,[3] corrosion inhibitors,[4] self-assembly monolayer (SAM),[5] inorganic coatings,[6] conducting polymeric coatings,[7] organic-inorganic coatings,[8] or any combination thereof, have been developed to address the growing need of copper corrosion inhibition in aggressive aqueous solutions. However, all these methods are subject to certain limitations, such as the high cost and hydrogen embrittlement occurrence of cathodic protection, the environmental toxicity of organic inhibitors,[9] poor durability and limited corrosion resistance of SAMs,[10] poor adhesion and water permeability of conducting polymer coatings.[11] Therefore, an alternative strategy is highly desirable to provide effective and long-lasting protection for copper corrosion.

Wetting behaviour, as one of the most important properties of a solid surface, has a significant effect on the service life, energy consumption and application scope of engineered materials. Inspired by water-repellent and self-cleaning behaviour of the micro- and nano-structured lotus surfaces, superhydrophobic surfaces, with a water contact angle (CA) larger than 150^o and sliding angle (SA) less than 10^o,[12] have received considerable interests in past decades, and have been extensively investigated as a superior solution to long-standing problems of corrosion of

[a]*Multiphase Mass Transfer & Reaction Engineering Lab, College of Chemical Engineering, Sichuan University, Chengdu, China 610065. Fax: 86 28 85460557; Tel: 86 28 85999978; E-mail: yuanshaojun@gmail.com*
[b] *Department of Mechanical and Materials Engineering, Masdar Institute of Science and Technology, PO Box 54224, Abu Dhabi, United Arab Emirates.E-mail: tjzhang@masdar.ac.ae*
[c] *Department of Environmental Sciences, University of Eastern Finland, 70211 Kuopio, Finland*
Electronic Supplementary Information (ESI) available: [details of any supplementary information available should be included here]. See DOI: 10.1039/b000000x/

metallic engineering.[13] Based on the concept that corrosion reactions are triggered by the contact of metal surfaces and water (as well as aggressive anions), the reduction in contact area between water and metallic substrates is considered to substantially retard the corrosion rate of engineered metals.[14] Due to their characteristics of water repellence and low adhesion, superhydrophobic coatings have been successfully employed on the surfaces of various engineered metals, such as copper,[1] aluminium,[15] magnesium,[16] zinc,[17] and stainless steel,[18] in enhancing their corrosion resistance by acting as an effective barrier to keep water, corrosive medium or humid atmosphere away from contacting and interacting with the metallic substrates. As wettability of a solid surface is governed by chemical compositions and geometrical structures, superhydrophobic surfaces can thus be achieved by two typical ways, either by creating hierarchical micro-/nano-structures on the hydrophobic substrates[19, 20] or by chemically modifying of an appropriate rough surface with low surface energy materials.[21] Based on this principle, various strategies have been developed to fabricate superhydrophobic surfaces on the metal substrates, such as chemical etching,[22, 23] sol-gel processing,[24] self-assembly,[25, 26] chemical vapour deposition,[27] electro-deposition,[28, 29] electro-spinning,[30] solution immersion,[31] plasma etching,[32] graft polymerization,[33] hydrothermal oxidation,[34] lithography,[35, 36] and anodization process.[37]. However, many of these methods have potential shortcomings for practical applications, such as time-consuming multistep processes, special equipments, toxic or expensive reagents, and uncontrollable geometric structures. In comparison, the anodization method is considered to be one of the most promising techniques to produce self-ordered nanostructures over large areas with the featured advantages of low cost, facile and rapid fabrication, easy scale-up, and precise control of surface roughness and nanostructures.[38] Anodic films are generally much stronger and more adherent than most of types of oxide layers from chemical etching, which makes them less likely to crack and peel from aging and wear.[39] Thereby, anodic films are believed to provide superior corrosion protective coatings to the underlying metallic substrates compared to other methods. However, few studies have been reported on the copper substrates, albeit that a few studies have reported for aluminium and titanium substrates.[40, 41].

Recently, considerable efforts have been devoted to synthesizing cupric oxide (CuO) nanostructures on copper substrates to fabricate superhydrophobic surfaces. As a *p*-type semiconductor with a narrow band gap (1.2 eV), CuO nanostructures, with large surface areas and superior physical and chemical properties, have been used as superconductors, anode electrodes for batteries, catalysis, energetic materials, sensors and superhydrophobic surfaces.[42] CuO nanostructures with different morphologies, such as nanoparticles, nanorods, nanowires, nanotubes, microcabbages-like patterns, dandelion-like and flower-like structures, have been extensively reported to grow on copper surfaces.[16, 42, 43] The typical synthesis methods of CuO nanostructures involve thermal oxidation,[44] solution immersion,[45] electro-deposition,[46] chemical oxidation,[47] and hydrothermal synthesis.[48] In addition, cupric hydroxide ($Cu(OH)_2$) nanomaterials with layered structures have also been reported to be used as precursors to synthesize homogeneous single-crystalline CuO nanoribbons and two-dimensional nanoleaves on a large scale.[49] The facile transformation of $Cu(OH)_2$ nanostructures to CuO nanostructures without obvious morphological changes can be readily achieved through dehydration by heat treatment.[50] As mentioned above, electrochemical anodization of copper in an alkaline aqueous solution is a facile and controllable method to synthesize dense and highly-ordered $Cu(OH)_2$ nanostructures with cost efficiency.[51] Some pioneering studies have successfully synthesized $Cu(OH)_2$ nanoneedle and nanotube arrays on copper surfaces by an anodization process in NaOH or KOH solutions,[51, 52] and the size and morphology of nanostructures may be accurately modulated by varying the electrochemical conditions.[53] Moreover, several previous studies have utilized the anodized $Cu(OH)_2$ nanostructures to fabricate superhydrophobic surfaces.[37, 54] It is well known that $Cu(OH)_2$ is a thermodynamically metastable phase, which can be easily transformed into more stable CuO.[55] This transformation is found to occur in a solid state by thermal dehydration at a relatively low temperature, and to take place in aqueous media at room temperature.[56] As a consequence, it is favorable to use CuO nanostructures rather than $Cu(OH)_2$ as stable templates to fabricate superhydrophobic copper surfaces. However, to the best of our knowledge, few previous studies have directly utilized anodic CuO nanostructures to fabricate superhydrophobic surfaces, especially for the anticorrosive behaviour of anodic CuO layers on the copper substrates.

Herein, the main aim of this study is to fabricate superhydrophobic CuO nanoneedle array (NNA) films on the copper substrate surfaces by a facile and controllable anodization method for corrosion inhibition in an aggressive chloride-containing solution. The clean copper foils were anodized in an aqueous KOH solution to grow CuO nanoneedle array (NNA) films by varying electrochemical anodization conditions. Surface fluorosilanization was subsequently conducted to introduce superhydrophobicity on the CuO NNA surfaces. Success in the fabrication of CuO NNA films and modification with fluoroalkylsilane (FAS-17) was ascertained by scanning electron microscope-energy dispersive X-ray analysis (SEM-EDS), X-ray diffraction (XRD), X-ray photoelectron spectroscopy (XPS) and water contact angle measurements. The wetting behaviours of superhydrophobic CuO NNA surfaces were characterized to determine the relationship of water contact angles, surface roughness, water contact angle hysteresis and the anodization time. The anticorrosion behaviour of superhydrophobic anodic CuO NNA coatings in a 3.5 wt.% NaCl solution was determined by the measurements of Tafel plots and electrochemical impedance spectroscopy (EIS) data. The durability and stability of the superhydrophobic CuO NNA films on the copper substrates were also evaluated by SEM observation and water

contact angle analyses. Overall, the main contribution of this study is summarized as follows: i) in previous studies,[37,54] the anodized $Cu(OH)_2$ nanostructures were used to fabricate superhydrophobic surface. However, the thermodynamic metastability of $Cu(OH)_2$ is a significant concern of superhydrophobic $Cu(OH)_2$ surfaces for anticorrosion applications in a harsh environment. In this work, the thermodynamic stable CuO NNA films are used as templates to create superhydrophobic surface for anticorrosion application. Few studies have been documented to investigate the anticorrosion behaviour of the superhydrophobic CuO nanostructured surfaces from electrochemical anodization. ii) Considering the water repellency and barrier effect, the Cassie-model suerphydrophobic surface is more favorable for the anticorrosion protection than the Wenzel-model one. However, few studies have been reported to correlate anticorrosion performance with the superwetting model of the coatings. This study utilizes the sliding angles and contact angle hysteresis to affirm the Cassie-model feature of the superhydrophobic CuO NNA surface. iii) Environmental scanning electron microscopy (ESEM) is used to evaluate the dynamic water contact angles of the superhydrophobic CuO NNA surface, which has been seldom reported previously. Additionally, the dependence of anticorrosion performance on the thickenss of the superhydrophobic CuO NNA is also investigated.

2. Experimental

2.1 Materials

Copper foils (99.9%, 0.1 mm thick) were purchased from Xingbo Metal Sample Co. (Tianjin, China). 1H, 1H, 2H, 2H-perfluorodecyltriethoxysilane (FAS-17, 97%) was obtained from Sigma-Aldrich Chem. Co. (St. Louis, MO). All the reagent-grade chemical reagents, such as KOH (85%), NaCl, and HCl (37%), and organic solvents, such as acetone, isopropyl alcohol, ethanol and tetrahydrofuran (THF, 95%) were purchased from Kelong Chem. Co. (Chengdu, China) and were all used as received. Ultrapure deionized water from Ulupure-II-20T water system (Chengdu, China) was used throughout the experiments.

2.2 Pretreatment of Copper Foils

The copper foils were cut into a dimension of 4 cm in length and 1 cm in width, polished with SiC paper of sequentially finer grit down to 1200 grit, and finally were washed with copious amounts of deionized water, ultrasonically degreased in acetone, isopropyl alcohol, ethanol and deionized water, in that order, for 15 min each to obtain the clean and grease-free surfaces. To remove the oxide layer from the copper surfaces, the clean newly-polished copper foils were immersed in a 2 mol L^{-1} HCl aqueous solution for 20 min at room temperature. The resultant copper surfaces were ultrasonically washed with copious amounts of deionized water, followed by being dried with nitrogen (N_2) stream and then stored in a vacuum desiccator.

2.3 Electrochemical Anodization to Grow $Cu(OH)_2$ Nanoneedle Array Films

The synthesis procedures of $Cu(OH)_2$ nanoneedle array (NNA) films were similar to those described in detail previously.[51] Briefly, the pretreated copper foils were used as the working electrode with a surface area of 2 cm^2 (half of copper foils immersed in an electrolyte solution), and a platinum (Pt) foils, surface area of 4 cm^2) as the counter electrode. The copper anode and Pt cathode were fixed in a one-compartment Teflon cell with a distance of 2 cm, and were subsequently connected to an AUTOLAB 128N potentiostat-galvanostat (Ecochemie Co., Netherlands) under computer control using NOVA 1.10 software. The typical electrolyte was an aqueous KOH aqueous solution, and the solution was deaerated by bubbling with dry N_2 stream for 30 min prior to anodization process. The reaction temperature was controlled by placing the Teflon electrolytic cell in a cryogenic thermostatic bath during the anodization process. To determine the optimal anodization conditions for the growth of $Cu(OH)_2$ NNA films, the anodization reaction was allowed to proceed at a constant current density over 0.5 – 4.0 mA cm^{-2} in a KOH solution concentration range of 0.5 – 4.0 mol L^{-1} at electrolyte temperature ranging between 5 ± 1° and 25 ± 1° for a typical 25 min. The anodization reaction at the optimal conditions was also conducted for anodization time ranging from 5 to 40 min to grow CuO NNA surfaces. After anodization, a faint-blue film was formed on the copper foils. Then the as-prepared copper foils were removed out from the solution and rinsed with copious amounts of deionized water, and finally were dried with pure N_2 stream prior to storage in a vacuum desiccator.

2.4 Formation of CuO NNA Films and Modification with Fluoroalkylsilane

The transformation of $Cu(OH)_2$ NNA into CuO NNA can be readily accomplished by a dehydration reaction. Typically, the $Cu(OH)_2$ NNA coupons was heated to 150 °C for 3 h to complete the dehydration, and then the temperature increased to 200 °C for another 3 h to promote crystallization under N_2 protection. The annealed copper coupons were naturally cooled to room temperature. The CuO NNA surfaces obtained from the 25 and 40 min of anodization reaction at a constant current density of 2 mA cm^{-2} in a 2.0 mol L^{-1} KOH solution at 15 ± 1°C were defined as the CuO NNA-1 and CuO NNA-2 surfaces, respectively. To fabricate superhydrophobic surfaces, the CuO NNA surfaces were modified by a fluorosilanization reaction. The fluoroalkylsilane solution was prepared by mixing 1 g of FAS-17 and 99 g of ethanol under continuous stirring at 150 rpm for 3 h. The copper coupons with CuO NNA films were immersed in the above fluoroalkylsilane solution at room temperature for 12 h, followed by washing with copious amounts of ethanol and deionized water, and then dried at 100 °C in a vacuum ov-

en for 1 h. The resulting FAS-modified CuO NNA surfaces were referred to as the CuO NNA-FAS surfaces.

2.5 Surface Characterization

The surface morphologies of the as-synthesized CuO NNA and FAS-modified CuO NNA films were characterized by SEM imaging on a FEI Quanta 250 SEM (Hillsboro, Oregon, USA) with a beam energy of 5.0 kV. The atomic composition was probed using an SEM equipped energy dispersive X-ray (EDS) spectrometer at a beam energy of 15.0 kV. The EDS mapping of fluorine (F), silicon (Si) and oxygen (O) elements for the FAS-modified surfaces was recorded to ascertain success in fluorosilanization reaction. X-ray diffraction (XRD) patterns of the CuO NNA films were obtained by using an X-ray diffractometer DX 2700 model (Haoyuan Instruments Co., Dandong, China) with Cu Kα radiation (λ = 1.5418 Å) to confirm the crystalline structures. The chemical compositions of the CuO NNA and FAS-modified CuO NNA surfaces were also characterized by X-ray photoelectron spectroscopy (XPS) on a VG Microlab MKII XPS spectrometer (VG Scientific, East Grinstead, UK) with a monochromatic Al Kα X-ray source (1486.6 eV photons) using procedures described in detail previously.[57] All the binding energy (BEs) data were calibrated with respect to the C 1s signal of ambient hydrocarbons (C-H and C-C species) at 284.6 eV. A multimode atomic force microscopy (AFM) equipped with a Nanoscope IIIa controller (Digital Instrument, Santa Barbara, CA) was used to capture AFM images with a scan size of 5 μm × 5 μm in contact mode in air. Nanoscope software was used to determine the root-mean-square (rms) roughness of the CuO NNA surfaces.

2.6 Wetting Behaviour on the Superhydrophobic CuO NAA Surfaces

The static and dynamic water contact angles of the superhydrophobic surfaces were measured on a DM 501 goniometer (Kyowa Interface Science Co. Saitama, Japan). Static contact angles were measured by a typical sessile drop method, which dropped a 3 μL droplet of deionized water onto the substrates. Advancing angle (θ_A) measurements were performed with a starting droplet of 2.5 μL and increasing the droplet volume at 0.5 μL s^{-1} until the droplet volume reached 7.5 μL. Subsequently, receding angle (θ_R) measurements were performed by decreasing the volume of a 7.5 μL droplet in 0.5 μL s^{-1} until the droplet reached the initial 2.5 μL. The values reported are averages of at least five measurements made on different locations over the copper substrates. The difference between the advancing and receding angles is contact angle hysteresis. The sliding angles (SA) were measured to tilt the surface with a water droplet of 5.0 μL. Sequence photographs of the sliding behaviour of the water droplets on the inclined surface (of 1°) were taken every 33 ms. The dynamic water contact angle profiles on the superhydrophobic surfaces were also studied using an environmental scanning electron microscopy (ESEM, FEI Quanta 250, Hillsboro, Oregon) with a beam energy of 10.0 kV. A Gaseous SED detector was used for the ESEM mode. In situ observation of water droplets formed on the superhydrophobic surfaces was achieved by maintaining the sample temperature at 2 °C and increasing chamber pressure to 750 Pa.

2.7 Anticorrosion Behaviour of the Superhydrophobic CuO NAA Films

The anticorrosion performance was evaluated by means of Tafel plots and electrochemical impedance spectroscopy (EIS) test using a conventional three-electrode cell with a capacity of 500 mL. The platinum foil was served as the counter electrode, Ag/AgCl/KCl (3 mol L^{-1}) as the reference electrode, and the copper coupons with an exposed area of 2 cm^2 as the work electrode. In all cases, the corrosion experiments were carried out under aerated conditions by exposing the copper coupons in a 3.5 wt% NaCl solution for 1 and 7 days. The measurements of Tafel plots and EIS spectra were performed on the AUTOLAB 128N electrochemical workstation. The potentiodynamic Tafel plots were obtained at a scan rate of 1 mV s^{-1} in a range of ±250 mV versus the open circuit potential (OCP). The EIS data were recorded at OCP using a 10 mV amplitude sinusoidal signal in a frequency range of 10^5 to 0.005 Hz. The inhibition efficiency (η) of the superhydrophobic CuO NNA coupons with respect to the pristine Cu substrates can be calculated using the following equation,

$$\eta\% = \frac{j_o - j_{corr}}{j_o} \quad (1)$$

where j_o and j_{corr} were the corrosion current densities of the pristine Cu and the modified Cu coupons, respectively, as determined from the analysis of Tafel plots. The corrosion rate (ν) can be calculated from the following equation:[11]

$$\nu = \frac{j_{corr} \cdot K \cdot E_w}{d \cdot A} \quad (2)$$

where, K is a constant that defines the units for ν, and A, d, and E_w are the sample area (2 cm^2), the density (8.89 g cm^{-3}) and equivalent weight (31.5 g mol^{-1}) of copper substrates, respectively.

2.8. The Stability of the Superhydrophobic CuO NAA Films

The stability of the superhydrophobic CuO NAA surfaces was determined by measuring the change in static water contact angles with exposure time in the pure water, 1.5wt.% and 3.5 wt% aqueous NaCl solution. SEM images of the superhydrophobic CuO NAA surfaces were captured after a predetermined exposure time in a 3.5 wt% aqueous NaCl solution to evaluate the geometric structure change of the superhydrophobic surface.

3. Results and Discussion

The hirarchical micro-/nanostructure and low surface energy materials are prerequisites to fabricate superhydrophobic surfaces. In the current study, a two-step fabrication process is used to fabricate superhydrophobic

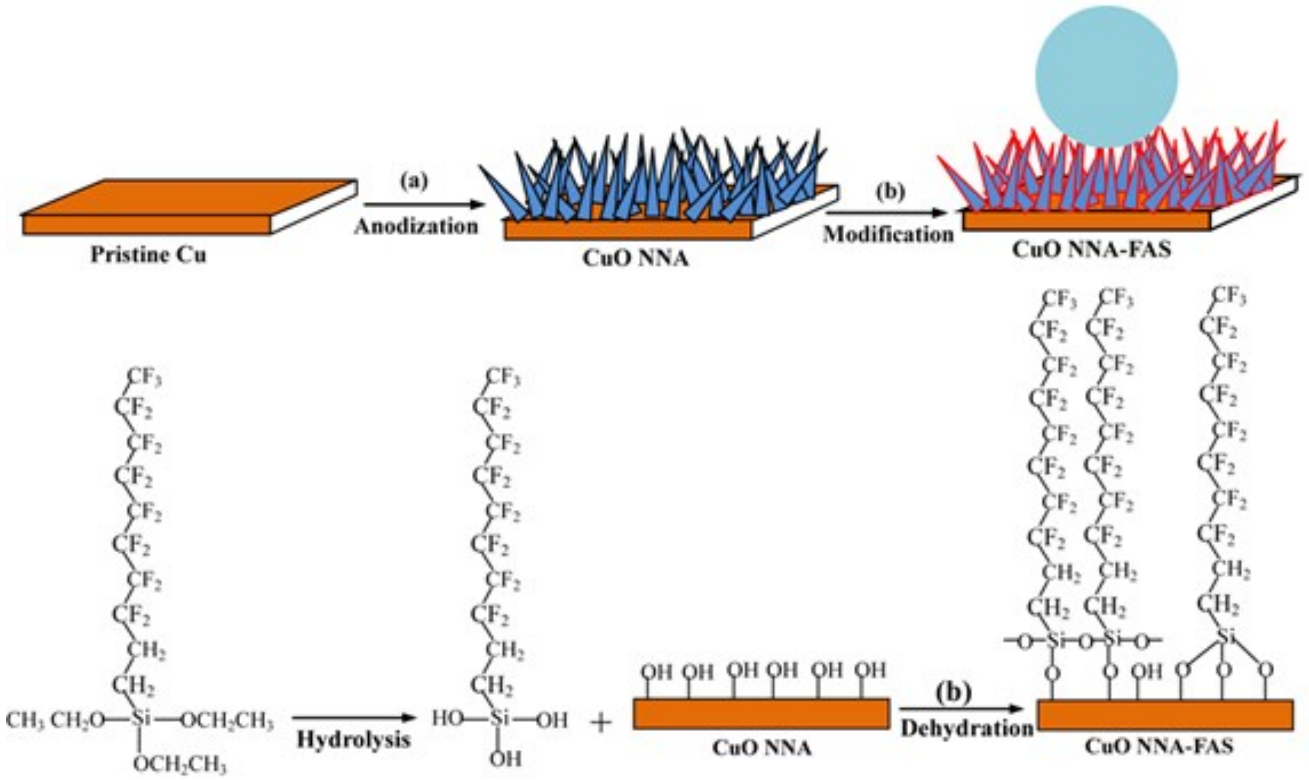

Fig. 1 Schematic illustration of the two-step fabrication process of superhydrophobic CuO nanoneedle array (NNA) surfaces: (a) the anodization process to grow CuO NNA films on the Cu substrates, and (b) the fluorosilanization of the CuO NNA films to create superhydrophobic Cu substrates (referred to as the CuO-NNA-FAS surface).

CuO nanoneedle array (NNA) films on copper foil surfaces, as shown schematically in Figure 1. The synthesis of CuO NNA films is achieved by the growth of $Cu(OH)_2$ NNA via electrochemical anodization in a KOH solution and the transformation of $Cu(OH)_2$ into CuO by a dehydr-ation reaction. Subequent fluorosilanization of CuO NNA films with FAS-17 endows the copper substrates with the desired low surface energy to obtain a superhydrophobic surface. The hydrolysis of triethoxysilane precursor occurs first to produce active silanol groups, and then the interfacial con-densation and cross-linking reactions take place between the hydroxyl groups of the CuO NNA films and the silanol groups, leading to a robust covalent binding between the organic layers and the copper substrates. The details of each fabrication step are discussed below.

3.1 Growth of CuO NNA Films on Copper Substrates

Electrochemical anodization, as a well-established fabrication method, has been investigated to grow the orthohombic $Cu(OH)_2$ nanowires in a alkaline (NaOH or KOH) aqueous solution.[37, 51, 54] Generally, the formation mechanism of the anodic CuO nanostructures is involved in the following electrochemical reaction and the dehydration reaction:[52]

$$Cu\,(s) \rightarrow Cu^{2+} + 2e^{-} \quad (3)$$

$$Cu^{2+} + 2OH^{-}(aq) \rightarrow Cu(OH)_2(s) \quad (4)$$

$$Cu(OH)_2(s) \rightarrow CuO\,(s) + H_2O \quad (5)$$

The elecrochemical reaction 3 is the anodic oxidation reaction to produce Cu^{2+} ions, which is accompanied by the cathodic hydrogen evolution reaction. The nucleation of $Cu(OH)_2$ takes place at the localized regions of supersaturared Cu^{2+} ions and hydroxyl ions (OH^{-}), as indicated in reaction 4. To achieve the CuO nanostructues, the as-prepared $Cu(OH)_2$ nanomaterials are subject to the dehydration reaction by annealing at 120 – 150 ^{o}C.The surface morphology remained unchanged during the transfromation of $Cu(OH)_2$ into CuO by the annealing dehydration reaction.[54]

In this study, the electrochemical anodization protocol was conducted sequentially by varying the KOH concen-tration, reaction temperature and current density to obtain the optimized anodization conditions for the growth of CuO NNA films on the copper surfaces. The results of the effect of KOH concentration, reaction temperature and current density on the anodization synthesis of CuO NNA films have been discussed in detail in the Supporting Information (S1.1 – S1.3, Figures S1 – S3). The optimized anodization conditions are chosen as the KOH conencen-tration of 2 mol L^{-1}, reaction temperature of 15 $\pm$ 1 ^{o}C, and a current density of 2.0 mA cm^{-2}. The growth of CuO NNA films was performed at the above optimized anodization conditions for different reaction time.

3.1.1. SEM Images. Figure 2 shows the typical SEM images of the CuO NNA films on the copper surfaces after anodizing in a 2 mol Ł$^{-1}$ KOH solution at a constant current density of 2.0 mA cm^{-2} at 15 ± 1 °C for 5, 25 and 45 min. The electrolysis time has an clear effect on the growth of Cu NAA films on the copper surfaces in the length and the number density of nanoneedles. After anodizing for 5 min, only some individual CuO nanoneedles with an average length of 2 – 4 μm are sparsely distributed over the copper surfaces (Figures 2a and 2b), indicating that the $Cu(OH)_2$ nanoneedles require sufficient time to nucleate and crystalize together with the electrolysis reaction. As the electrolysis time increases to 25 min, the copper surface is covered with dense and compact pine-needle-like CuO NNA films (Figures 2c and 2d). The length of CuO nanoneedles increase to about 7 – 10 μm and the sharp tips of the nanoneedles are 170 ± 40 nm in average diameters (Figure 2d). Upon prolonging the electrolysis time to 40 min, the average length of nanoneedles undergoes a further increase to 10 –15 m and the average diameter of the sharp tips of the nanoneedles increases to 190 ± 50 nm (Figures 2e and 2f). The above results indicate that the CuO NNA films can be successfully grown on the copper surface after anodizing of the copper foil for a sufficient reaction time (i.e., longer than 25 min). In this study, the as-prepared CuO NNA obtained after anodizing for 25 and 40 min are defined as the CuO NNA-1 and CuO NNA-2 surfaces, respectively, for the subsequent studies. Except for the increase in the size and the number density of CuO nanoneedles with electrolysis time, prolonging the electrolysis time can also result in an increase in the thickness of CuO NNA films. Figures 3a and 3b show the side-view SEM images of the CuO NNA-1 and CuO NNA-2 surfaces obtained after anodizing in a 2 mol Ł$^{-1}$ KOH solution for 25 and 40 min, respectively. The thickness of the CuO NNA-1 films is around 7 μm (Figure 3a), while that of the CuO NNA-2 films is around 12 μm (Figure 3b). The hierarchical structure of CuO nanoneedles and the inherent hydrophilic properties of CuO leads to a superhydrophilic CuO NNA surface, as the static water contact angle on the CuO NNA-1 surface is less than 5° (Inset of Figure3c).

3.1.2 EDS and XPS Spectra. The chemical composition of the CuO NNA surface was characterized by the EDS and XPS measurements to confirm the presence of CuO. Figure 3d shows the corresponding EDS spectrum of the CuO NAA-1 surface. The component atoms are ascertained to be Cu and O elements from the EDS spectrum. The relative atomic ratio of [Cu]/[O] is determined to be 1.2:1.0 (calculated from 54.4:45.6), which is comparable to the stoichiometric value of 1:1 for cupric oxide.

Figures 3e and 3f show the wide scan and Cu 2p core-level XPS spectra of the CuO NNA-1 surface, respectively. The photoelectron lines at binding energies (BEs) of 77, 285, 530, 570 and 930 eV, attributable to Cu 3p, C 1s, O 1s, Cu LMM and Cu 2psignals,[58] respectively, are observed in the wide scan spectrum of the CuO NNA surface (Figure 3). The [Cu]:[O] ratio, as determined from the sensitivity-factor-corrected Cu 2p and O 1s core-level spectral area, is approximately 1.0:1.1, which is close to the theoretical value of 1.0:1.0 for cupric oxide. The Cu $2p_{3/2}$ core-level spectrum can be curve-fitted into two peak components at BEs of 933.5 and 935.6 eV, attributable to CuO and $Cu(OH)_2$ species,[58] respectively (Figure 3f). The predominant peak component of CuO in the Cu $2p_{3/2}$ spectrum is consistent with the formation of cupric oxide on the anodized copper surface. This point is further confirmed by the curve-fitted O 1s spectrum of the CuO NNA-1 surfaces (Supporting Information, Figure S4a), which consists of the predominant oxide (BE at 529.6 eV), hydroxide (BE at 531.2 eV) and trace water (BE at 532.6 eV).[57] The presence of $Cu(OH)_2$ compounds on the CuO NNA surface is probably associated with, at least in part, the adsorption of water molecules during sample handling. The presence of a C 1s signal, consisting of the three peak components of C-H (284.6 eV), C-O (286.2 eV) and O=C-O (288.5 eV), is ascribed to the adsorption of adventitious carbon and hydrocarbon on the CuO NNA surfaces (Supporting Information, Figure S4b). The above XPS results are consistent with the fact that cupric oxides have successfully formed on the CuO NNA surfaces.

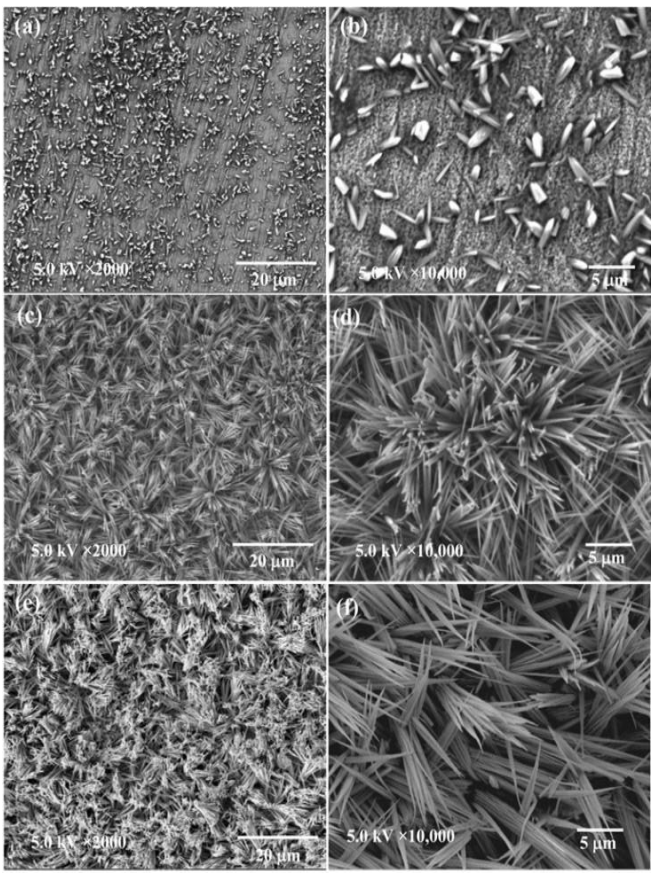

Fig. 2 Representative SEM images at low (×2000) and high (×10000) magnifications of the CuO NNA surfaces after anodizing in a 2.0 mol Ł$^{-1}$ KOH solution at 15 ± 1°C at a constant current density of 2.0 mA cm^{-2} for different anodization time: (a,b) 5 min, (c, d) 25 min, and (e,f) 40 min.

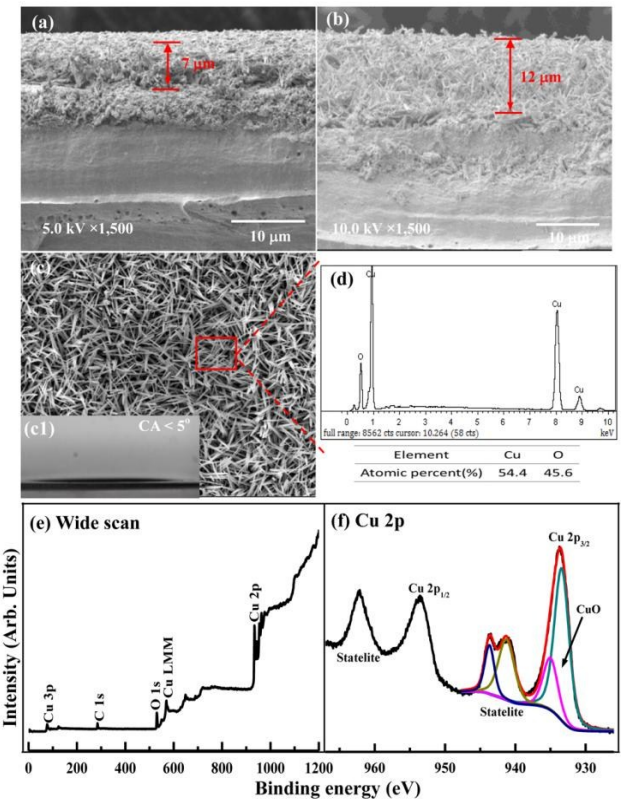

Fig. 3 Side view SEM image (×1500) of the CuO NNA-1 and CuO NNA-2 surfaces after anodizing for (a) 25 min and (b) 40 min, respectively, at a constant current density of 2.0 mA cm^{-2} at 15 ± 1°C in a 2.0 mol L^{-1} KOH solution. Images (c) and (d) correspond to the top view SEM images of the CuO NNA-1 surface and the corresponding EDS spectrum, (e) Wide scan and (f) Cu 2p core-level XPS spectra of the CuO NNA-1 surface.

3.1.3. XRD Patterns. XRD analysis was further performed to confirm the formation of crystalline CuO nanoneedles on the anodized copper surface. Figure 4 shows the XRD pattern of the CuO NNA films after anodizing in a 2.0 mol L^{-1} KOH solution for different time. The diffraction peaks marked with solid circles are attributed to the Cu substrates (Supporting Information, Figure S5), while the weak diffraction peaks marked with asterisk at 2θ of 35.5° (002) and 38.7° (111) are attributed to the monoclinic phase of CuO (JCPDS card No. 05-0661) (Figures 4b and 4c). The wide diffraction peaks at 35.5° and 38.7° reveal that the CuO nanoneedles are polycrystalline in nature.[51] The absence of crystalline CuO diffraction peaks for the bare Cu and the CuO NNA surface from 5 min of anodization suggests that the crystalline CuO is generated by anodization process rather than oxidization in air, and that the sparsely-distributed and the low number density of CuO nanoneedles from 5 min of anodization are insufficient to be detected by XRD. The XRD results are consistent with the above SEM, EDS and XPS results that the hierarchical and dense CuO NNA films have been successfully fabricated by the electrochemical anodization and the dehydration reaction on the copper substrates.

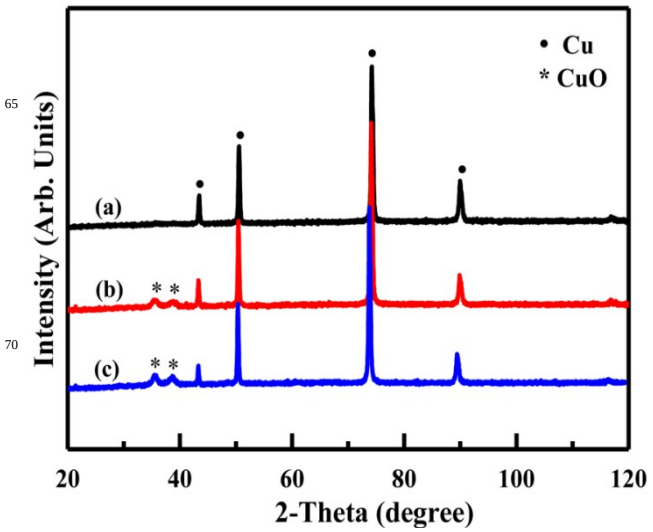

Fig. 4 XRD patterns of the CuO NNA surfaces after anodizing in a 2.0 mol L^{-1} KOH solution at a constant current density of 2.0 mA cm^{-2} at 15 ± 1°C for (a) 5 min, (b) 25 min and (c) 40 min.

3.2 Fabrication of Superhydrophobic CuO NNA Surfaces. The introduction of low surface energy materials was performed by a self-assembly fluorosilanization reaction to create the superhydrophobicity on the hierarchical CuO NNA surfaces. In this study, FAS-17, which contains the terminal $–CF_3$ group (with a surface energy of 6.7 mJ m^{-2}) and $–CF_2$ groups (with a surface energy of 18 mJ m^{-2}), was used to reduce the surface energy of CuO NNA surfaces while maintaining surface roughness. The resultant FAS-modified surfaces from 25 min of anodization are defined as the CuO NNA-1-FAS surfaces.

3.2.1. SEM-EDS. Figures 5a-5d show the SEM images and the corresponding EDS spectrum and elemental mapping of the CuO NNA-1-FAS surfaces, respectively. Although the FAS-modified CuO NNA surfaces show some changes in the geometric structures, the CuO nanoneedles can still be clearly observed to maintain their micro- and nano-structures (Figures 5a and 5c), since only a self-assembled fluorosilane monolayer is immobilized on the CuO NNA surface. The introduction of FAS-17 onto the CuO NNA-1 surfaces can be ascertained by the EDS spectrum, which is obtained on a random area of the substrates. The FAS-modified surface consists mainly of O, Cu, F, C and Si elemental signals (Figure 5b). The additional elements of F, C and Si, as compared to that on the CuO NNA surfaces, indicate the presence of FAS-17 on the substrates. The relative atomic ratio of [F]:[Si] is around 17.4:1, which is close to the theoretical value of 17:1 of the FAS-17 molecular structure. The EDS elemental mapping images of F and Si demonstrates the uniform distribution of FAS-17 on the CuO NNA surface (Figure 5d). Moreover, the overlapped EDS mapping is consistent with the uniform distribution of the self-assembled FAS-17 on the CuO NNA surface.

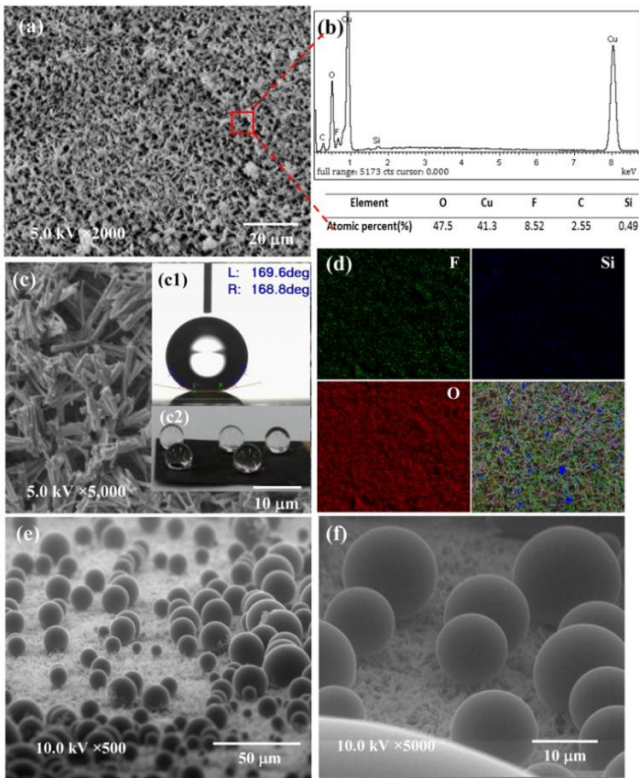

Fig. 5 SEM images of the CuO NNA-1-FAS surfaces at the low (a, ×2000) and high (c, ×5000) magnifications, (b) the EDS spectrum and (d) the elemental maps of F, Si, O and the element-overlapped map of a random area on the FAS-modified surfaces, and (e,f) ESEM images of the contact angle profiles of water droplets on the CuO NNA-1-FAS surfaces at the low (×500) and high (×5000) magnifications. Insets (c1) and (c2) represent water contact angles and optical images of water droplets at different locations of the CuO NNA-1-FAS surfaces, respectively.

3.2.2. Contact Angle Analysis. The change in surface wettability further confirms the successful immobilization of FAS-17 to create the superhydrophobic CuO NNA surface. The persistence of the geometric structures of the CuO nanoneedles after the fluorosilanization is essential for superhydrophobicity. The combination of the low surface energy fluorosilane and surface roughness (arising from the nanoneedles) leads to a superhydrophobic surface, as the static water contact angle of the CuO NNA-1-FAS surface reaches as high as approximately 169^{o} (Inset, Figure 5c1). The optical images of water droplets at different locations of the CuO NNA-1-FAS surface suggest uniform surface superhydrophobicity (Inset, Figure 5c2). The ESEM observations give insight into the dynamic wetting behaviour at the micrometer-sized water droplets on a solid surface.[59] Figures 5e and 5f capture the remarkable close-up ESEM images of the microscale droplet profiles on the CuO-NNA-1-FAS surfaces. Various micrometer-sized water droplets from 3 – 30 μm in size are essentially spherical and are clearly suspended on the top of the CuO-NNA-FAS surfaces, where the rough microstructures are also visible, demonstrating that the superhydrophobicity has been created down to micrometer dimensions on the CuO NNA surfaces.

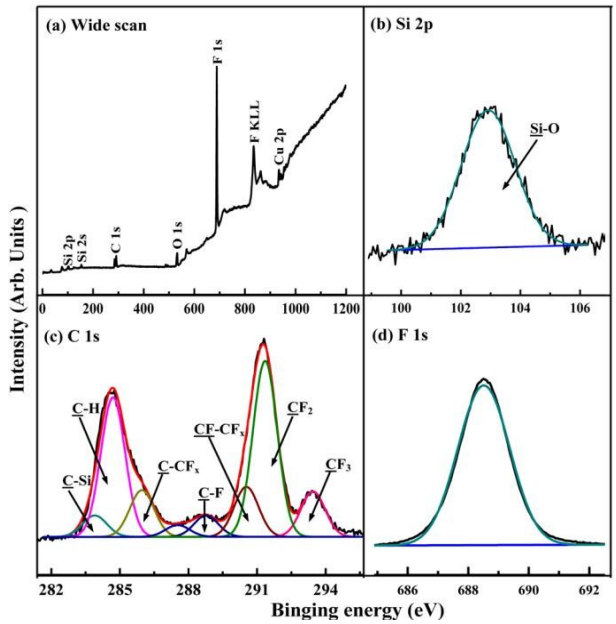

Fig. 6 (a) Wide scan XPS spectra of the CuO NNA-1 surfaces and the FAS-modified CuO NNA-1 surfaces, (b) Si 2p, (c) C 1s and (d) F 1s core-level XPS spectra of the FAS-modified CuO NNA-1 surfaces.

3.2.3. XPS Spectra. The chemical composition of the CuO-NNA-1-FAS surface was characterized to further ascertain the immobilization of FAS-17 on the substrates. Figure 6 shows the wide scan, Si 2p, C 1s and F 1s core-level XPS spectra of the CuO NNA-1-FAS surface. In comparison with the wide scan spectrum of the CuO NNA surface, four additional photoelectron lines at BEs of about 99, 151, 685, and 832 eV, attributable to Si 2p, Si 2s, F 1s and F $KL_{23}L_{23}$ species, respectively, are observed in the wide scan spectrum of the CuO NNA-1-FAS surface (Figure 6a). The [F]/[Si] ratio, as determined from the sensitivity-factor-corrected F 1s and Si 2p core-level spectral area, is around 0.056, comparable to the theoretical value of 0.059 of the FAS-17 molecules. The curve-fitted C 1s core-level spectrum consists of seven peak components with BEs at 283.8, 284.6, 286.0, 288.8, 290.5, 291.4 and 293.4 eV, attributable to C-Si, C-H, C-CF_x, C-F, CF-CF_x, C-F_2, and C-F_3 species,[60] respectively (Figure 6c). The fluorine peak components of C-CF_x, C-F, CF-CF_x, C-F_2, and C-F_3 are characteristics of the FAS-17 molecule. The only peak component appearing at a BE of about 689 eV in the F 1s core-level spectrum is associated with C-F species[58] (Figure 6d). The single Si 2p peak component with a BE at about 102.8 eV is associated with Si-O species[58] (Figure 6b), indicating that the FAS monolayer is immobilized on the CuO NNA surface via the robust Si-O bonds. Thus, the FAS-17 monolayer has been successfully immobilized on the CuO NNA surfaces.

3.3 Wetting Behaviour of the Superhydrophobic CuO NNA Surfaces

The wetting behaviour of the resultant superhydrophobic surfaces prepared at different anodization time was evaluated by static water contact angle and contact angle hysteresis. Figure 7a shows the change in static water contact angles and surface roughness with anodization time. Within the first 15 min of anodization, surface roughness undergoes a large increase from 0.75 ± 0.12 μm for 5 min of anodization to 1.92 ± 0.15 μm for 15 min of anodization. Then, the increase in surface roughness slows down and reaches a platform after 25 min of anodization with a surface roughness of 2.24 ± 0.12 μm. Correspondingly, the change in water contact angles has a similar tendency with anodization time from about 137 ± 2° for 5 min of anodization, 165 ± 2° for 15 min and 168 ± 1° f or 40 min of anodization. The static water contact angle appears to be dependent on the surface roughness from various anodization time. The water contact angle change can be understood theoretically by the Cassie-Baxter equation:[61]

$$\cos\theta_r = f_1 \cos\theta - f_2 \quad (6)$$

where θ and θr represent the contact angles of flat copper surface and the rough copper surface with FAS-modified CuO NNA, respectively, f_1 and f_2 are the fractions of solid surface and air in contact with air, respectively (i.e. $f_1 + f_2=1$). Since the θ value of a fluorosilanized flat copper surface is almost constant to be around 113° (Supporting Information, Figure S6). The higher surface roughness can trap more air in the hierarchical needle-like microstructures to reduce the f_1 value, thus leading to a larger contact angle for a superhydrophobic surface. As shown in Figure 7b, the change in contact angle hysteresis with anodization time has an opposite trend to that of the water contact angle. The contact angle hysteresis is about 39 ± 2° for 5 min of anodization. Upon prolonging the anodization time to 10 min, the contact angle hysteresis decreases dramatically to about 14 ± 1° on a superhydrophobic surface with static water contact angles of 156 ± 1°. The contact angle hysteresis reaches to a minimum value of around 5 ± 0.4° with anodization time longer than 15 min, at which the surface roughness reaches a maximum value. Thus, the high surface roughness from a longer anodization time is directly associated with a superhydrophobic surface with a contact angle of higher than 165° and contact angle hysteresis of less than 5°.

To confirm the consistency of the superhydrophobic CuO NNA surface with the Cassie-Baxter model, the sliding angle profiles are captured on the CuO NNA-1-FAS surface with a droplet volume of 5 μL at a tilted angle of 1°, and the images are shown in Figure 8. The smooth sliding of the water droplet over the entire CuO NNA-1-FAS surface demonstrates that no pinning of water droplets inside the needle-like microstructures occurs on such superhydrophobic surfaces. It has been widely recognized that the air trapped in the surface structures plays a significant role for a surface with a low sliding angle.[62] The needle-like structures on the CuO NNA-FAS surface may serve as a means of trapping sufficient air for low sliding angles to be exhibited.

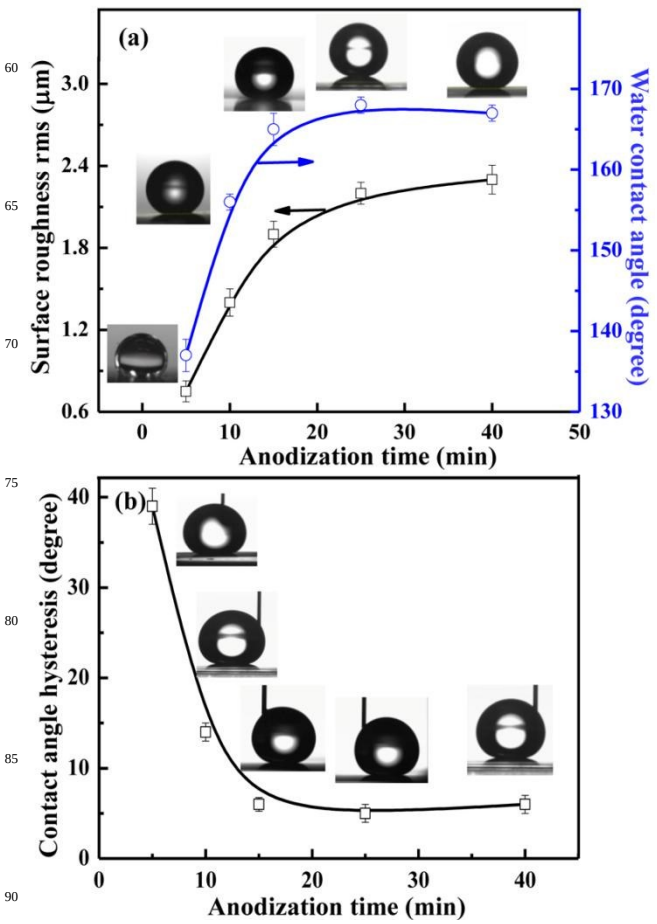

Fig. 7 (a) The changes in surface roughness of the CuO NNA surfaces and the water contact angles of the corresponding FAS-modified CuO NNA surfaces as a function of anodization time, (b) the relationship between water contact angle hysteresis of the FAS-modified CuO NNA surfaces and anodization time.

3.4 Anticorrosive Behaviour of the Superhydrophobic CuO NNA Surfaces

3.4.1 Tafel plots. Tafel plots have been widely used to monitor the instantaneous corrosion rate of a metal or alloy exposed to a corrosive environments and to determine the change in corrosion rates due to the presence of coatings, inhibitors or bacteria.[7] Tafel plots of the pristine and surface-modified Cu coupons were obtained to evaluate their anticorrosive behaviour in a NaCl solution for various exposure periods. Figure 9 shows the respective Tafel plots of the pristine Cu, CuO NNA, and FAS-modified CuO NNA coupons after 1 and 7 days of exposure in a 3.5 wt.% NaCl solution. Tafel plots are further analyzed by extrapolating the linear anodic and cathodic branches to their intersection to obtain corrosion current densities (j_{corr}), corrosion potentials (E_{corr}, vs. Ag/AgCl/3 mol L^{-1} KCl), Tafel slopes (b_a and b_c), and polarization resistance (R_p) using procedures described previously.[60] The analytical parameters are summarized in Supporting Information Table S1.

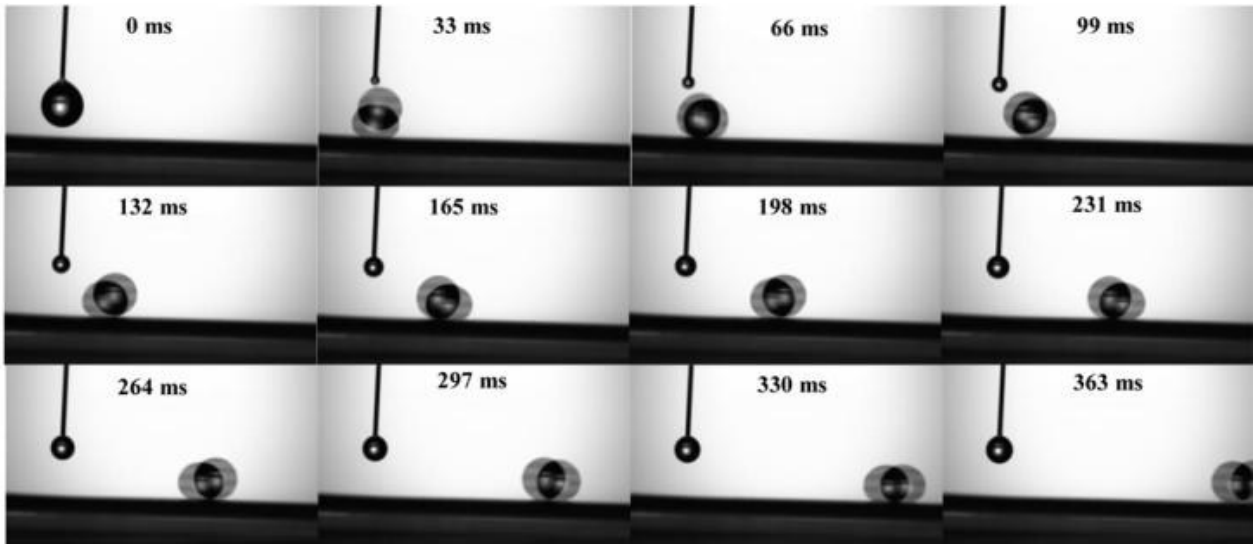

Fig .8 Sliding behaviour of a water droplet on the FAS-modified CuO NNA-1 surfaces with the operation conditions: droplet volume of 5 μL, tilt angle of surface of 1°, high-speed photography with 33 ms/frame.

For the pristine Cu coupons, the values of corrosion current density, j_{corr}, show an evident decrease from 19.6 to 14.4 μA cm^{-2} with increasing exposure time from 1 day to 7 days, which is ascribed to the formation of protective oxide films (mainly consisting of Cu_2O) on the substrates. This result is consistent with previous finding that the protective Cu_2O films formed in chloride media can retard the anodic dissolution of unalloyed copper.[63] The j_{corr} values of the CuO NNA coupons are much smaller than that of the pristine Cu coupon during the initial 1 day of exposure, indicative of the protective nature of the anodic CuO nanoneedle films. Meanwhile, the E_{corr} values of the CuO NNA-1 and CuO NNA-2 coupons exhibit a positive shift to about -227 and -212 mV, respectively, which is probably associated with the anodic protection in terms of the mixed potential theory.[64] However, the j_{corr} values of the CuO NNA coupons increase by approximately 27% relative to the initial values after 7 days of exposure, suggesting that the protective capability of the anodic CuO NNA films is compromised by the prolonged attack of aggressive chloride ions (Cl^-). The heterogeneous and porous features of the anodic CuO nanoneedles are favorable for the local attack of the aggressive Cl^- to initiate the localized corrosion. Moreover, the CuO NNA-2 coupons appear to perform slightly better than the CuO NNA-1 coupons in decreasing corrosion of the underlying Cu substrates, as the j_{corr} values of the CuO NNA-2 coupons always remain slightly smaller than those of the CuO NNA-1 coupons throughout the exposure periods. This result is probably caused by the formation of a thicker and more compact anodic CuO NNA films on the CuO NNA-2 coupons. Consequently, the inhibition efficiencies (η) of the CuO NNA-1 and CuO NNA-2 coupons, calculated from equation (1), are around 48.2% and 53.5%, respectively, after the initial 1 day of exposure. They have dramatically decreased to about 10.4% and 19.8%, respectively, after 7 days of exposure, further demonstrating a limited protective capability of the anodic CuO-nanoneedle films.

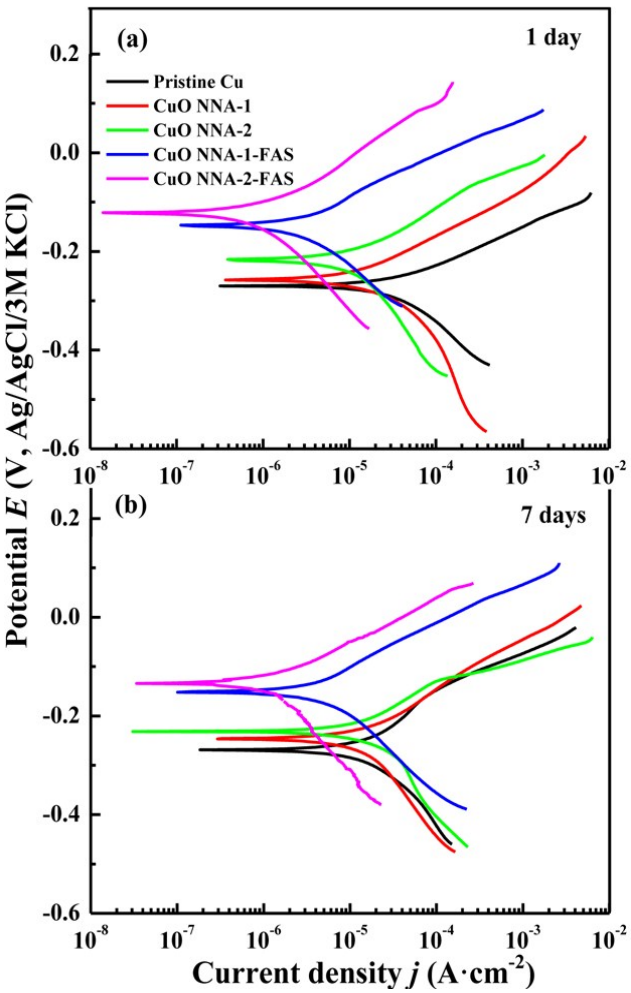

Fig. 9 Tafel plots of the pristine Cu, CuO NNA-1, CuO-NNA-2, CuO NNA-1-FAS, and CuO NNA-2-FAS coupons after exposure in a 3.5% NaCl solution for (a) 1 day and (b) 7 days.

In the case of the superhydrophobic FAS-modified CuO NNA coupons, the corrosion potential, E_{corr}, shows a marked positive shift to more noble values as compared to those of the pristine and CuO NNA coupons, and remains relatively constant throughout the exposure periods (Supporting Information, Table S1). These results are ascribed to the barrier effect and water repellency of the superhydrophobic fluorosilanized CuO NNA films. The ennoblement in the corrosion potential is a common phenomenon derived from the anodic protection of organic coatings for metal coupons.[65] The significantly smaller values in the corrosion current density of the FAS-modified coupons are observed throughout the exposure periods (Figure 9). The j_{corr} magnitude for the CuO NNA-1-FAS and CuO NNA-2-FAS coupons is lower by about 10- and 12-fold, respectively, as compared to that of the corresponding CuO NNA coupons after 7 days of exposure in a 3.5 wt.% NaCl aqueous solution, indicating that the superhydrophobic fluorosilanized CuO nanoneedle films render the desired protection capability to the underlying copper substrates against corrosion. Furthermore, the protection capability of the CuO NNA-2-FAS coupons appears to be more pronounced than that of the CuO NNA-1-FAS coupons, as the former possesses thicker and more compact fluorosilanized CuO nanoneedle films, while the surface superhydrophobicity is similar. As a result, the inhibition efficiency (η) of the CuO NNA-1-FAS coupons remains higher than 90% throughout the experiment, while that of the CuO NNA-2-FAS coupons is always higher than 93% throughout the exposure periods (Supporting Information, Table S1). It is logical to conclude that the anticorrosion capability originates from the water repelling property and the physical diffusion barriers of the superhydrophobic CuO nanoneedle films. The barrier behaviour of the polymeric coatings has been found to be associated with their thickness, compactness and geometric structures, as well as the chemical properties of the employed polymer molecules.[60]

3.4.2 EIS spectra. EIS is a nondestructive and useful technique to characterize electrochemical reactions and subprocesses occurring at the metal/electrolyte interfaces, and provides important information regarding the reaction mechanisms and kinetics of a coating/electrolyte system.[66] Figure 10 shows Nyquist plots and Bode modulus plots of the pristine Cu and surface-modified Cu coupons after 1 and 7 days of exposure in a 3.5 wt.% aqueous NaCl solution. The EIS data are further fitted by using the Boukamp's EQUIVCRT program with an appropriate equivalent electrical circuit (EEC). Three EECs are proposed to fit the respective EIS data of the bare and surface-modified copper coupons as schematically shown in Supporting Information Figure S8. EEC (a) is used to model a single charge transfer reaction with a Warburg element for the pristine Cu substrates after 1 day of exposure. EECs (b) and (c) contain two time constants, and have been widely used to fit the EIS data of a metal substrate with organic/inorganic coatings. The fitted parameters are summarized in Supporting Information Table S2.

For the pristine Cu coupon, the Nyquist loop consists of a semicircle and a linear tail at the low frequency region after 1 day of exposure (Inset, Figure 10a1). The linear portion, which inclines at an angle of 45° to the real axis, is defined as the Warburg impedance due to a diffusion control process. The diffusion control process is associated with either the transfer of Cl^- to copper substrates or the transfer of the chloride-copper complexes of $CuCl_2^-$ or $CuCl_4^{2-}$ to the bulk solution during the copper corrosion process.[2] At the same time, the diameters of Nyquist semicircles increase with exposure time (Inset, Figure 10c1). The charge transfer resistance, R_{ct}, of the pristine Cu coupons increases rapidly from about 250 Ohm cm^{-2} to 410 Ohm cm^{-2} after 7 days of exposure due to the formation of oxide films (Supporting Information, Table S2). As for the anodic CuO NNA coupons, the diameters of the Nyquist loops undergo a gradual decrease with an increase in exposure time from 1 to 7 days (Figures 10a and 10c1), indicative of the gradual loss in passivity of the anodic CuO NNA films. The Bode modulus plot of the CuO NNA films appears second time constant after 1 day of exposure (Figure 10b), indicative of the penetration of water to the copper substrates. This result is consistent with the fact that the CuO NNA films are porous and thin oxide layers, which is readily penetrated inside by aggressive medium.This point is further confirmed by the marked decrease in the resistance of anodic CuO NNA films, R_f, with exposure time. Generally, the corrosion process is strongly dependent on the diffusion of corrosive species, such as Cl^-, through the pores of coatings and also the removal of corrosion products from the substrate surface in to expose fresh surface for a further attack. Thus, the significant decrease in the resistance of anodic CuO nanoneedle film indicates the loss of the barrier property and the robust permeability of aggressive Cl^- ions to the copper substrates.

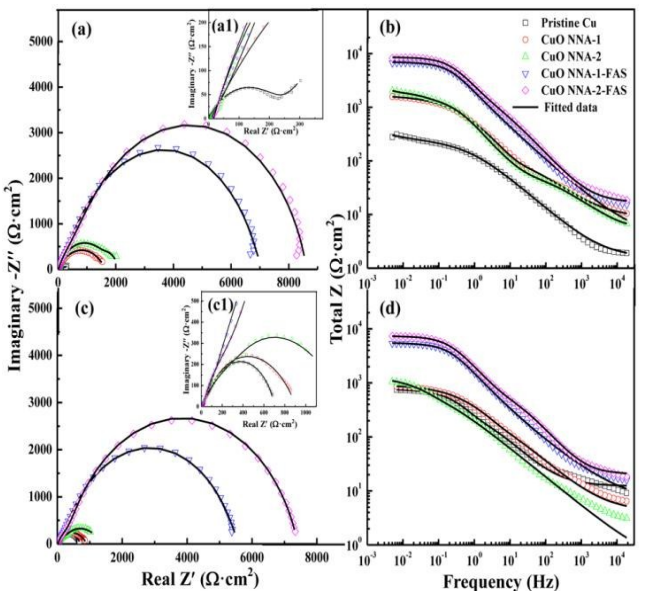

Fig. 10 Nyquist plots and Bode magnitude plots of the bare Cu, CuO NNA-1, CuO NNA-2, CuO NNA-1-FAS, and CuO NNA-2-FAS coupons after exposure in a 3.5 wt.% NaCl solution for (a,b) 1 day and (c,d) 7 days. The insets (a1) and (c1) are the magnified Nyquist plots of the pristine Cu coupons in the high frequency range after 1 and 7 days of exposure, respectively.

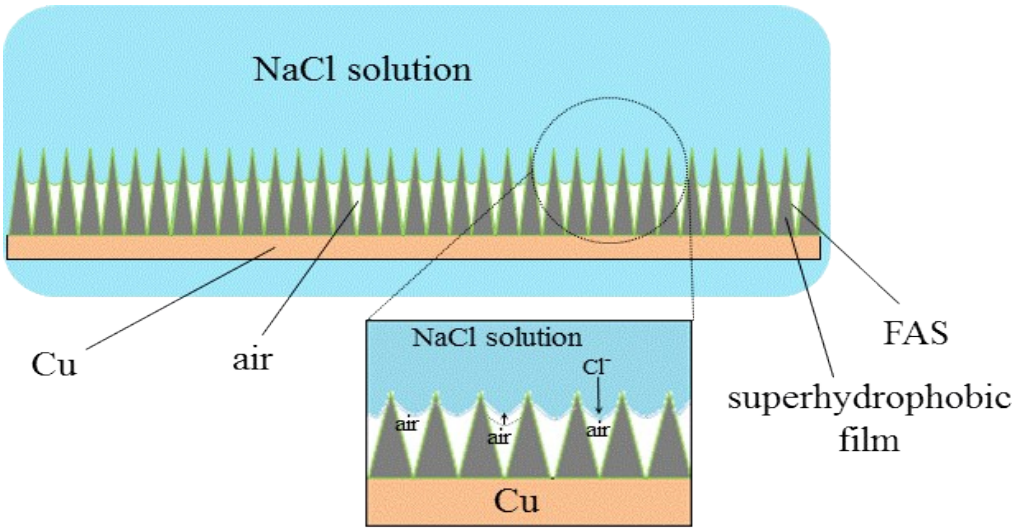

Fig. 11 Model of the interface between superhydrophobic CuO NNA surface and a 3.5 wt% NaCl aqueous solution (solid-liquid interface)

As for the superhydrophobic FAS-modified CuO NNA coupons, the diameters of the Nyquist loops are significantly larger than those of the pristine Cu and CuO NNA coupons throughout the exposure periods, and undergo a slight decrease with exposure time, indicative of the highly enhanced corrosion resistance of copper substrates (Figures 9a and 9c). The magnitude of the Bode modulus plots of the superhydrophobic coupons is larger by more than one order of magnitude than that of the pristine Cu and CuO NNA coupons (Figures 9b and 9d). Moreover, the Bode modulus at the lowest frequency, $|Z|_{0.01Hz}$, which is also used to estimate the corrosion activity, remains generally stable for the CuO NNA-1-FAS and CuO NNA-2-FAS coatings after 1 day of exposure, suggesting that the aggressive species have not reached the alloy surface.[67] After 7 days of exposure, three important characteristics at low frequencies, including steady $|Z|_{0.01Hz}$ value, pure capacitive feature and no emergence of additional time constant, confirm that the CuO NNA-FAS films still keep intact.[67] The values of charge transfer resistance, R_{ct}, of the superhydrophobic CuO NNA-1-FAS and CuO NNA-2-FAS coupons are larger by at least 3.5- and 4.5-fold than those of the corresponding CuO NNA coupons (Supporting Information, Table S2), indicative of the substantial improvement in the protective capability of fluorosilanized CuO NNA films. The resistance of superhydrophobic CuO NNA-FAS films, R_f, remains high throughout the exposure periods, demonstrating the low permeability, high water repellency, and a good physical barrier property of the fluorosilanized CuO NNA films. However, both the values of R_{ct} and R_f of the superhydrophobic CuO NNA-FAS coupons show a slight decrease after 7 days of exposure, implying the compromised water repelling ability and barrier property of the superhydro-phobic CuO NNA-FAS films under the attack of aggressive Cl^- anions. The capacitance value of the CuO NNA-FAS films, Q_f (constant phase element of coatings), appears to increase with increasing the exposure time (Supporting Information, Table S2), suggesting that water has probably penetrated inside the superhydrophobic CuO NNA films after 7 days of exposure. The phenomenon is probably caused by the changes in surface geometric structures and superhydrophobicity of the CuO NNA-FAS surfaces. On the other hand, the R_{ct} and R_f values of the CuO NNA-2-FAS coupons are always larger than those of the CuO NNA-1-FAS coupons, demonstrating that the thickness of the FAS-modified CuO NNA films plays a significant role in conferring the physical barrier and anticorrosion capability on the copper substrates. Generally, the thicker the CuO NNA-FAS film is, the more air is trapped in the pores between the CuO NNA fims. Thus, the higher anticorrosion capability of the CuO NNA-2-FAS films is attributed to the thicker CuO NNA layers and more air trapped inside the pores between the CuO NNA layers.

3.5 Anticorrosion Mechanism of Superhydrophobic CuO NNA Films

As discussed above, the superhydrophobicity of the CuO NNA surfaces is virtually consistent with the Cassie-Baxter model, of which water droplets are suspended on the rough surface to trap air within the grooves. Figure 11 shows a schematic interface model to illustrate the liquid-solid interfaces between the superhydrophobic CuO NNA surface and NaCl solution. The superhydrophobic CuO nanoneedle-covered surface consists of unique nanoneedle and valley structures. Such structures can trap the air inside the valleys between nanoneedles, thus leading to the substantial increase in surface air fraction in the valleys and the reduction of actual surface area in contact with the aqueous NaCl solution. The air layers inside the valleys, together with the superhydrophobic CuO NNA layers, can not only act as an effective barrier to prevent the aggressive Cl^- ions from approaching the bare copper substrates, but also substantially enhance the corrosion resistance of superhydrophobic CuO NNA layers due to the good insulation property of air.

As the matter of fact, the anticorrosion performance of the superhydrophobic CuO NNA surfaces may also be associated with capillary effect. It is well known that when a vertical cylindrical tube is placed in a liquid phase, the liquid rises and forms a concave surface (i.e. meniscus) in a hydrophilic tube due to the intermolecular force between the liquid and surrounding solid surface. However, if the tube is hydrophobic, the liquid would be depressed. The height (h) of a liquid column is given by the following equation: [68]

$$h = (2\gamma \cos \theta)/\rho g r \quad (7)$$

where γ is the liquid-air surface tense, θ is the contact angle, ρ is the density of liquid, g is local acceleration due to gravity, and r is radius of cylindrical tube. Thus, the thinner the space in which the water can travel, the further up it goes in a hydrophilic tube. On contrary, the capillary effect is significantly descending based on the fact that the superhydrophobic CuO NNA surface has a high contact angle (>160^o) and the pore diameter is fairly small. Moreover, in such minute pore structures, the liquid could transport against gravity. As a result, the NaCl aqueous solution can be pushed out from the minute pores of superhydrophobic CuO NNA films by Laplace pressure. In light of the previous EIS data, the superhydrophobic CuO NNA layers can prevent the corrosion reaction from processing owing to the presence of air layer within the minute pores, as well as the physical presence of superhydrophobic CuO NNA layers.

3.6 The Stability and Durability of Superhydrophobic CuO NAA Films.

The problem of superhydrophobicity degradation becomes extremely significant in view of the extended areas of application of hydrophobic and superhydrophobic materials and coatings.[69] The stability and durability of the superhydrophobicity of protective coatings is an important criterion in assessing the performance of superhydrophobic surface in corrosion protection.[70] Figure 12 shows the changes in water contact angles of the CuO NNA-1-FAS surface as function of pH values and exposure time in pure water, 1.5 wt.% NaCl and 3.5 wt.% NaCl solution, respectively. The effect of salt (NaCl) concentrations was also determined to evaluate the stability of the superhydrophobic CuO NNA surface (Supporting Information, Figure S7). As shown in Figure 12a, the values of water contact angles remain larger than 165^o in a wide pH range of 3 – 13, albeit of a slight decrease to 157 ± 1^o in water contact angle at pH 1, demonstrating the stable superhydrophobicity of the CuO NNA-1-FAS surface. The water contact angles of the CuO NNA-1-FAS surface even show a slight increase with increase in the concentration of NaCl solution (Supporting Information, Figure S7). The superhydrophobic CuO NNA-FAS surface shows a remarkable stability in pure water, as the water contact angle remains almost unchanged at more than 165^o throughout the exposure periods (Fig. 12b). Similarly, the stable superhydrophobicity of the CuO NNA-FAS surface can also be observed after exposed to a 1.5 wt.% NaCl solution throughout.

After the CuO NNA-1-FAS coupons exposed to the 3.5 wt.% NaCl solution, the surface superhydrophobicity remains almost unchanged during the initial 3 days, as the water contact angles are higher than 163^o. The superhydrophobicity can even persist upon prolonging the exposure time to 6 days, as the water contact angle is approximately 151^o after 6 days of exposure. However, the CuO NNA-1-FAS surface appears to lose its superhydrophobicity after 7 days of exposure, since the static water contact angle decreases to about 148^o. Different mechanisms have been proposed to interpret the loss of superwettability of the superhydrophobic surfaces,, including the growth of adsorption/wetting films, surface hydrophilization due to chemical interactions, the nonreversible hydration of hydrogen bonding active groups inside the hydrophobic and superhydrophobic materials, and the changes in the surface roughness and microstructures.[60, 69, 71]

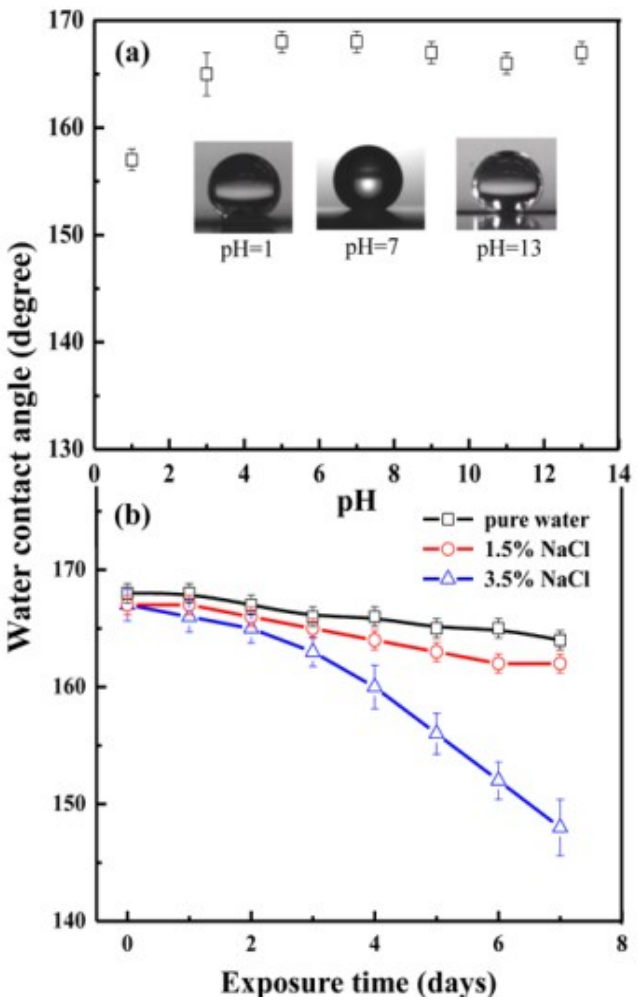

Fig. 12 The change in water contact angles of the Cu -NNA-1-FAS surfaces as a function of (a) pH and (b) exposure time in pure water, 1.5 wt.% NaCl and 3.5 wt.% NaCl solutions.

The change in surface morphologies of the CuO NNA-1-FAS coupons was determined to find out the reason for the loss of surface superhydrophobicity. The top-view SEM images of the CuO NNA-1-FAS coupons after 3 and 7 days of exposure in a 3.5 wt.% NaCl solution were shown in Supporting Information (Figure S8). The hierarchical needle-like microstructures remain almost unchanged after 3 days of exposure (Figure S8a), hence, it displays a stable superhydrophobic surface with a water contact angle of about 163°. With increasing the exposure time to 7 days, the geometric microstructures of the CuO NNA-FAS surface undergo a marked change (Figure S8b), as the CuO nanoneedles appear to be flatten and become amalgamated with the scales mainly derived from salt crystallization (Figure S8c) The loss of hierarchical microstructures is believed to be the main culprit to the degradation of superhydrophobicity of the CuO NNA film. On the other hand, it is worthwhile to note that the CuO NNA-FAS surface still remains highly hydrophobic and provides superior anticorrosive function. Therefore, further studies focusing on the long-term anticorrosive performance of the FAS-modified CuO NNA films in aggressive chloride-containing aqueous media are in progress to evaluate the maximum time of corrosion protection.

4. Conclusions

With the objective of fabricating superhydrophobic CuO nanoneedle array (NNA) films on the copper substrates for superior anticorrosion protection, a two-step process by the combination of a facile and controllable anodization process and fluorosilanization was described. The hierarchical CuO NNA films with different surface roughness and thickness were grown by anodization in an aqueous KOH solution with the optimized electrolysis conditions. Subsequent fluorosilanization was performed to create superhydrophobic surfaces with water repelling and anti-corrosion properties. The successful fabrication of a superhydrophobic hierarchical CuO NNA surfaces was confirmed by SEM imaging, XRD, EDS, XPS and water contact angle analyses. The wetting behaviour of the superhydrophobic CuO NNA surfaces was investigated to elucidate the relationship between static water contact angle, surface roughness, contact angle hysteresis, and anodization time. The resultant superhydrophobic CuO NNA surfaces were found to have a water contact angle as high as approximately 169° and contact angle hysteresis as low as about 5°. Electrochemical results demonstrated superior corrosion protection performance of the superhydrophobic CuO NNA surfaces with inhibition efficiency higher than 90% in aggressive chloride-containing media. The alteration in surface geometric structures of the FAS-modified CuO NNA surfaces was directly related to the deterioration of surface superhydrophobicity upon prolonging the exposure time in aqueous NaCl solution.

Associated content

Supporting Information. SEM images of CuO nanostructured surface obtained at different electrolyte concentration (Figure S1), reaction temperature (Figure S2), and current densities (Figure S3) via electrochemical anodization, XPS spectra of the CuO NNA-1 surfaces (Figure S4), XRD pattern of the pristine Cu substrates (Figure S5), and water contact angle profiles on the pristine Cu and FAS-modified Cu surfaces (Figure S6), the contact angle profile of the CuO NNA-1-FAS coupons of different concentration of NaCl solution (Figure S7), the surface morphologies of the CuO NNA-1-FAS coupons after different exposure time in NaCl solution (Figure S8), the proposed equivalent circuit to fit EIS data (Figure S9), analytical results of Tafel plots in Table S1, Fitted parameters of EIS data in Table S2.

Acknowledgment

The authors would like to acknowledge the financial assistance of key project of National Natural Science Foundation of China (NO. 21236004), and to thank for the support by the Cooperative Agreement between the Masdar Institute of Science and Technology, UAE and the Massachusetts Institute of Technology (MIT), USA.

Notes and Reference

1. T. Liu, S. Chen, S. Cheng, J. Tian, X. Chang and Y. Yin, *Electrochim. Acta*, 2007, **52**, 8003.
2. A. El Warraky, H. El Shayeb and E. Sherif, *Anti-corros. Method M.* 2004, **51**, 52.
3.R. Subasri, T. Shinohara and K. Mori, *J. Electrochem. Soc.* 2005, **152**, B105.
4. D. A. Winkler, M. Breedon, A. E. Hughes, F. R. Burden, A. S. Barnard, T. G. Harvey and I. Cole, *Green Chem.* 2014, **16**, 3349.
5. Y. M. Lee, Y. H. Chang Chien, M. K. Leung, C. C. Hu and C. C. Wan, *J. Mater. Chem. A* 2013, **1**, 3629.
6. D. Prasai, J. C. Tuberquia, R. R. Harl, G. K. Jennings and K. I. Bolotin, *ACS nano*, 2012, **6**, 1102.
7. G. P. Shumakovich, G. V. Otrokhov, M. E. Khlupova, I. S. Vasil'eva, E. A. Zaitseva, O. V. Morozova and A. I. Yaropolov, *RSC Adv.* 2014, **4**, 30193..
8. E. Abdullayev, V. Abbasov, A. Tursunbayeva, V. Portnov, H. Ibrahimov, G. Mukhtarova and Y. Lvov, *ACS Appl. Mater. Inter.* 2013, **5**, 4464.
9. M. Antonijevic and M. Petrovic, *Int. J. Electrochem. Sci*, 2008, **3**, 1.
10. A. Alagta, I. Felhösi, I. Bertoti and E. Kálmán, *Corros.Sci.* 2008, **50**, 1644.
11. S. Yuan, S. Pehkonen, B. Liang, Y. Ting, K. Neoh and E. Kang, *Corros.Sci.* 2010, **52**, 1958
12. E. Celia, T. Darmanin, E. Taffin de Givenchy, S. Amigoni and F. Guittard, *J. Colloid Interf. Sci.* 2013, **402**, 1.
13. T. Ishizaki and M. Sakamoto, *Langmuir*, 2011, **27**, 2375.
14. A. C. C. de Leon, R. B. Pernites and R. C. Advincula, *ACS Appl. Mater. Inter.* 2012, **4**, 3169-3176.
15. J. Liang, Y. Hu, Y. Wu and H. Chen, *J. Nanomater.* 2013, **2013**, 1.
16. Z. She, Q. Li, Z. Wang, L. Li, F. Chen and J. Zhou, *ACS Appl. Mater. Inter.* 2012, **4**, 4348.
17. H. Liu, S. Szunerits, M. Pisarek, W. Xu and R. Boukherroub, *ACS Appl. Mater. Inter.* 2009, **1**, 2086-2091.
18. K. C. Chang, H. I. Lu, C. W. Peng, M. C. Lai, S. C. Hsu, M. H. Hsu, Y. K. Tsai, C. H. Chang, W. I. Hung, Y. Wei and J. M. Yeh, *ACS Appl. Mater. Inter.* 2013, **5**, 1460-1467.
19. J. A. Lee and T. J. McCarthy, *Macromolecules*, 2007, **40**, 3965.
20. I. S. Bayer, A. J. Davis and A. Biswas, *RSC Adv.* 2014, **4**, 264.

21. N. Saleema, D. K. Sarkar, D. Gallant, R. W. Paynter and X. G. Chen, *ACS Appl. Mater. Inter.* 2011, **3**, 4775.
22. J. Ou, W. Hu, M. Xue, F. Wang and W. Li, *ACS Appl. Mater. Inter.* 2013, **5**, 3101.
23. L. Li, V. Breedveld and D. W. Hess, *ACS Appl. Mater. Inter.* 2012, **4**, 4549.
24. S. S. Latthe, C. Terashima, K. Nakata, M. Sakai and A. Fujishima, *J. Mater. Chem. A* 2014, **2**, 5548.
25. Y. Rahmawan, L. Xu and S. Yang, *J. Mater. Chem. A* 2013, **1**, 2955.
26. A. Checco, A. Rahman and C. T. Black, *Adv. Mater.* 2014, **26**, 886.
27. C. R. Crick, J. C. Bear, P. Southern and I. P. Parkin, *J. Mater. Chem. A* 2013, **1**, 4336.
28. A. Haghdoost and R. Pitchumani, *Langmuir* 2013, **30**, 4183.
29. S. Khorsand, K. Raeissi and F. Ashrafizadeh, *Appl. Surf. Sci.* 2014, **305**, 498.
30. B. Grignard, A. Vaillant, J. de Coninck, M. Piens, A. M. Jonas, C. Detrembleur and C. Jerome, *Langmuir*, 2011, **27**, 335..
31. T. Ishizaki and N. Saito, *Langmuir*, 2010, **26**, 9749.
32. N. M. Oliveira, R. L. Reis and J. F. Mano, *ACS Appl. Mater. Inter*. 2013, **5**, 4202.
33. B. J. Sparks, E. F. Hoff, L. Xiong, J. T. Goetz and D. L. Patton, *ACS Appl. Mater. Inter*. 2013, **5**, 1811.
34. H. J. Choi, J. H. Shin, S. Choo, J. Kim and H. Lee, *J. Mater. Chem. A* 2013, **1**, 8417.
35. Y. Li, J. John and K. Carter, *Adv. Funct. Mater.* 2014 (in press).
36. J. Y. Shiu, C. W. Kuo, P. Chen and C. Y. Mou, *Chem. Mater.* 2004, **16**, 561.
37. D. D. La, T. A. Nguyen, S. Lee, J. W. Kim and Y. S. Kim, *Appl. Surf. Sci.* 2011, **257**, 5705
38. T. Darmanin, E. T. De Givenchy, S. Amigoni and F. Guittard, *Adv. Mater.* 2013, **25**, 1378-1394.
39. C. Jeong and C. H. Choi, *ACS Appl. Mater. Inter*. 2012, **4**, 842.
40. T. He, Y. Wang, Y. Zhang, T. Xu and T. Liu, *Corros.Sci.* 2009, **51**, 1757.
41. F. Zhang, S. Chen, L. Dong, Y. Lei, T. Liu and Y. Yin, *Appl. Surf. Sci.* 2011, **257**, 2587.
42. Q. Zhang, D. Xu, T. F. Hung and K. Zhang, *Nanotechnology*, 2013, **24**, 065602.
43. J. Liu, X. Huang, Y. Li, Z. Li, Q. Chi and G. Li, *Solid State Sci.* 2008, **10**, 1568.
44. S. M. Lee, K. S. Kim, E. Pippel, S. Kim, J. H. Kim and H. J. Lee, *J. Phys. Chem. C* 2012, **116**, 2781.
45. F. Su and K. Yao, *ACS Appl. Mater. Inter.* 2014, **6**, 8762.
46. Q. Zhang, K. Zhang, D. Xu, G. Yang, H. Huang, F. Nie, C. Liu and S. Yang, *Prog. Mater. Sci* 2014, **60**, 208.
47. N. Zhang, S. Lu, W. Xu and Y. Zhang, *New J. Chem.* 2014 **38**, 4534.
48. F. Shi, X. Chen, L. Wang, J. Niu, J. Yu, Z. Wang and X. Zhang *Chem. Mater.* 2005, **17**, 6177-6180.
49. H. Xu, W. Wang, W. Zhu, L. Zhou and M. Ruan, *Cryst. Growth Des.* 2007, **7**, 2720.
50. X. Chen, L. Kong, D. Dong, G. Yang, L. Yu, J. Chen and P. Zhang, *J. Phys. Chem. C* 2009, **113**, 5396.
51. X. Wu, H. Bai, J. Zhang, F. E. Chen, G. Shi, *J. Phys. Chem. B* 2005**, 109,** 22836.
52. D. D. La, S. Y. Park, Y. W. Choi and Y. S. Kim, *B. Kor. Chem. Soc.* 2010, **31**, 2283-
53. N. Liu, D. Wu, H. Wu, F. Luo and J. Chen, *Solid State Sci.* 2008, **10**, 1049.
54. X. Wu and G. Shi, *J. Phys. Chem. B* 2006, **110**, 11247.
55. Y. Cudennec and A. Lecerf, *Solid State Sci.* 2003, **5**, 1471.
56. D. P. Singh, A. K. Ojha and O. N. Srivastava, *J. Phys. Chem. C* 2009, **113**, 3409.
57. S. J. Yuan and S. O. Pehkonen, *Colloid Surf. B* 2007, **59**, 87.
58. J. F. Moulder, W. F. Stickle, P. E. Sobol and K. D. Bomben, *Handbook of X-ray photoelectron spectroscopy*, Perkin Elmer Eden Prairie, MN, 1992.
59. A. Liukkonen, *Scanning*, 1997, **19**, 411.
60. S. J. Yuan, S. O. Pehkonen, B. Liang, Y. P. Ting, K. G. Neoh and E. T. Kang, *Corros.Sci.* 2011, **53**, 2738.
61. A. B. D. Cassie and S. Baxter, *Trans. Faraday Soc.* 1944, **40**, 546.
62. M. Miwa, A. Nakajima, A. Fujishima, K. Hashimoto and T. Watanabe, *Langmuir* 2000, **16**, 5754.
63. G. Kear, B. Barker and F. Walsh, *Corros. Sci.*, 2004, **46,** 109.
64. D. A. Jones, *Principles and prevention of corrosion*, Macmillan Publishing Co., 1991.
65. F. Mansfeld, *J. Appl. Electrochem.* 1995, **25**, 187.
66. F. Mansfeld, S. Jeanjaquet and M. Kendig, *Corros.Sci.* 1986, **26**, 735.
67. J. Fu, T. Chen, M. Wang, N. Yang, S. Li, Y. Wang and X. Liu, *ACS Nano*, 2013, **7**, 11397.
68. G. K. Batchelor. *An introduction to fluid dynamics*, Cambridge University Press, 2000.
69. L. Boinovich, A. M. Emelyanenko and A. S. Pashinin, *ACS Appl. Mater. Inter.* 2010, **2**, 1754.
70. L. Boinovich, S. Gnedenkov, D. Alpysbaeva, V. Egorkin, A. Emelyanenko, S. Sinebryukhov and A. Zaretskaya, *Corros.Sci.* 2012, **55**, 238.
71. J. Zimmermann, F. A. Reifler, U. Schrade, G. R. Artus and S. Seeger, *Colloid Surf. A* 2007, **302**, 234.